metals

Article

Improving Surface Roughness and Printability of LPBF Ti6246 Components Without Affecting Their Structure, Mechanical Properties and Building Rate

Thibault Mouret [1], Aurore Leclercq [1], Patrick K. Dubois [2] and Vladimir Brailovski [1,*]

[1] Department of Mechanical Engineering, École de Technologie Supérieure, Montreal, QC H3C 1K3, Canada
[2] Createk Innovation Group, University of Sherbrooke, Sherbrooke, QC J1K 0A5, Canada
* Correspondence: vladimir.brailovski@etsmtl.ca

Abstract

Laser powder bed fusion (LPBF) is the best suited technology to manufacture temperature-resistant Ti-6Al-2Sn-4Zr-6Mo parts with complex geometrical features for high-end applications. Improving printing accuracy by reducing the layer thickness (t) generally requires repeating a tedious and time-consuming process optimization routine. To simplify this endeavour, the present work proposes three process equivalence criteria allowing to transfer optimized process conditions from one printing parameter set to another. This approach recommends keeping the volumetric laser energy density (VED) and hatching space-to-layer thickness ratio (h/t) constant, while adjusting the scanning speed (v) and hatching space (h) accordingly. To validate this approach, Ti6246 parts were printed with 50 µm and 25 µm layer thicknesses, while keeping VED = 100 J/mm^3 and h/t = 3 constant for both cases. The printed samples were analyzed in terms of their density, microstructure and mechanical properties, as well as the geometric compliance of wall-, gap- and channel-containing artefacts. Highly dense samples exhibiting comparable microstructures and mechanical properties were obtained with both parameters sets investigated. However, they induced markedly differing geometric characteristics. Notably, using 25 µm layers allowed printing walls as thin as 0.2 mm as compared to 1.0 mm for 50 µm layers.

Keywords: additive manufacturing; laser powder bed fusion; titanium alloy; printability; thin features; internal channels

1. Introduction

The use of additive manufacturing (AM) technologies is currently on the rise as their high versatility and agility enable small series manufacturing, which is economically unsustainable using conventional processes [1,2]. Based on the sequential layer-by-layer shape forming principle, these technologies allow the manufacture of intricate and complex shapes with a significant reduction of overall material waste [3]. One of the best-known metal AM processes, laser powder bed fusion (LPBF), has been shown to be the most efficient technology for printing high density parts with small design features. The process uses fine powders (20–50 µm) and generates narrow melt pools, thus achieving relatively high resolutions (0.1–0.2 mm) and tight tolerances (±50 µm). Additionally, it is less expensive than its principal competitors, namely, electron beam powder bed fusion (EB-PBF) and directed energy deposition (DED) [4].

Academic Editors: Emanuela Cerri and Emanuele Ghio

Received: 24 November 2025
Revised: 19 December 2025
Accepted: 23 December 2025
Published: 27 December 2025

In the last decades, LPBF has been extensively used to print almost all categories of metallic materials, ranging from nickel [5], aluminum [6], iron [7] and titanium [8] alloys, and going all the way to refractory metals. Most of the LPBF-related literature focuses on the optimization of printing parameters (e.g., laser power, scanning speed, etc.) in a bid to minimize the occurrence of process-induced volumetric imperfections (e.g., pores, cracks, etc.) [9–11]. These optimization routines are mainly realized using bulk simply-shaped specimens, such as cylindrical or prismatic coupons [12]. However, to actually benefit from the outstanding potential of LPBF to manufacture complex and lightweight structures, another optimization target—the capacity to print high-precision small features in the form of walls, gaps and channels—must be considered.

Following the democratization of the LPBF process, a plethora of general printing recommendations have been advanced to improve the geometric compliance of printed parts [13] and to facilitate the removal of unmelted powder [14]. The quality and dimensional accuracy of LPBF parts are strongly influenced by surface orientation, slope and local geometrical features. For example, down-facing (downskin) surfaces, in particular, exhibit higher roughness due to dross formation and the adhesion of partially melted particles, with severity depending on the inclination angle and the heat dissipation capacity of the powder bed. Various strategies, such as contour scanning and angle-specific parameter optimization, have been demonstrated to improve surface quality, but they typically involve complex parameter sets and additional optimization efforts [15,16]. Some studies have also targeted the printing of different design features, including channels, lattices and thin walls. These have demonstrated the possibility of minimizing distortions of thin-walled structures by adequately positioning them relative to the recoater blade [17]. They have also revealed that shear forces induced by powder spreading during recoating operations could induce the failure of thin (~0.1 mm) walls [18]. Moreover, a lack of geometric compliance of thin-walled structures can be accompanied by local microstructure variations, which can in turn cause mechanical property variations as well [19]. Another technological challenge is the manufacture of channels parallel or slightly inclined to the building platform, since such design features frequently demonstrate significant distortions, including the collapse of down-facing surfaces [20,21]. Among the various potential solutions, reducing the layer thickness (t) represents the most straightforward and simplest approach to improve dimensional accuracy and surface quality. However, this strategy requires the definition of specific criteria to maintain the process productivity and material properties and minimize the cost and time associated with the search for new printing parameters.

Titanium alloys are of great interest in a variety of technological domains, including in the biomedical, petrochemical, automotive and aerospace industries, due to their excellent strength-to-weight ratio (>180 MPa/(g·cm^{-3})) [22,23], corrosion resistance [24,25] and biocompatibility [26,27]. The near-net shape manufacturing of complex parts enabled by AM processes reduces the buy-to-fly ratio of these expensive materials. While α + β Ti-6Al-4V alloy (Ti64) is one of the commonly used titanium alloys [28], the LPBF of other similar alloys has also been explored with the objective of meeting ever increasing application requirements. Recently, another α + β titanium alloy, Ti-6Al-2Sn-4Zr-6Mo (hereafter referred to as Ti6246), has attracted significant interest because of its high mechanical properties, especially at elevated temperatures. The unique properties of Ti6246 make it particularly interesting for applications in gas turbines, where the geometrical complexity of parts improving the performance of such engines justifies the use of LPBF as a manufacturing process.

The implementation of Ti6246 for the LPBF process started at the beginning of the present decade with the work of Carrozza et al., who were the first to report on the laser powder bed fusion printability of Ti6246 [29]. Other studies followed [30–32], highlighting the effects of process parameters, such as the laser power, scanning speed and hatching space, on the structural and mechanical properties of as-built Ti6246 parts. The works set out revealed the in-print formation of orthorhombic martensitic phase (α''), whose size and morphology varied as a function of process parameters. The studies aimed to understand the interaction between process parameters and structural and mechanical properties of printed materials, thus allowing the optimization of the process. The optimization was generally realized in two phases: (a) maximizing the as-printed density while forming the most appropriate as-printed microstructure [33] and (b) finding a compromise between process productivity and precision of printed parts. To achieve the latter, Carrozza et al. compared the printability of thin features and hollow channels using Ti64 and Ti6246 alloys. Compared to Ti64, Ti6246 was found to provide a better precision with thin features, but less with hollow channels [34]. In another study [35], the authors found that with its atypical α'' microstructure, Ti6246 provided a better accommodation of thermal stresses with a reduced risk of distortions than did Ti64.

The present work proposes improving the dimensional accuracy of Ti6246 components by using a simple and efficient layer thickness reduction strategy. However, to preserve the mechanical properties of printed parts and the laser build rate, a set of three process-equivalence criteria is introduced. Satisfying these criteria makes it possible to preserve similar melting conditions, while avoiding a costly and time-consuming re-optimization of other process parameters, including the laser powder, speed and hatching space. Next, to conclude on the impact of layer thickness variations on the geometric fidelity of printed parts, a series of artefacts containing thin wall/gap features and narrow channels was also printed using both layer thicknesses and compared with their original CAD files.

2. Materials and Methods

2.1. Powder and Printed Specimen

It is common knowledge that an adequate powder bed density and uniformity are essential to obtaining high quality LPBF parts, both in terms of printed density and geometric accuracy, and these outcomes depend significantly on the powder particle characteristics (size, sphericity, uniformity [36]). The gas-atomized pre-alloyed Ti6246 powder produced by Eckart TLS Gmbh (Bitterfeld-Wolfen, Germany) used in this study is highly spherical but with a certain amount of small satellite particles (see image in Figure 1a obtained using a Hitachi TM300 (Tokyo, Japan) scanning electron microscope). The initial powder particle size distribution (PSD) reported in [32] was measured using a Beckam Coulter LS13 320 XR particle size analyzer (Brea, CA, USA). To ensure that the powder was not mechanically segregated during recoating using a thinner layer thickness (25 µm), the PSDs inside three printer compartments, namely the dispensing and spreading platforms and the powder collector (Figure 1b), were measured for this layer thickness and found to be almost identical.

The powder was loaded into a Trumpf TruPrint 1000 LPBF system (TRUMPF GmbH, Ditzingen, Germany) (P = 200 W; laser spot size 55 µm). Based on the results of our previous study [32], the following optimized set of printing parameters was used in this study for a layer thickness t of 50 µm (referred to as Set I in Table 1): laser power P = 139 W, scanning speed v = 185 mm/s and hatching space h = 150 µm, resulting in a volumetric energy VED (1) = 100 J/mm^3, building rate BR (2) = 5 cm^3/h and h/t ratio = 3.

$$VED\left(\frac{J}{mm^3}\right) = \frac{P}{vht} \quad (1)$$

$$BR\left(\frac{cm^3}{h}\right) = vht \quad (2)$$

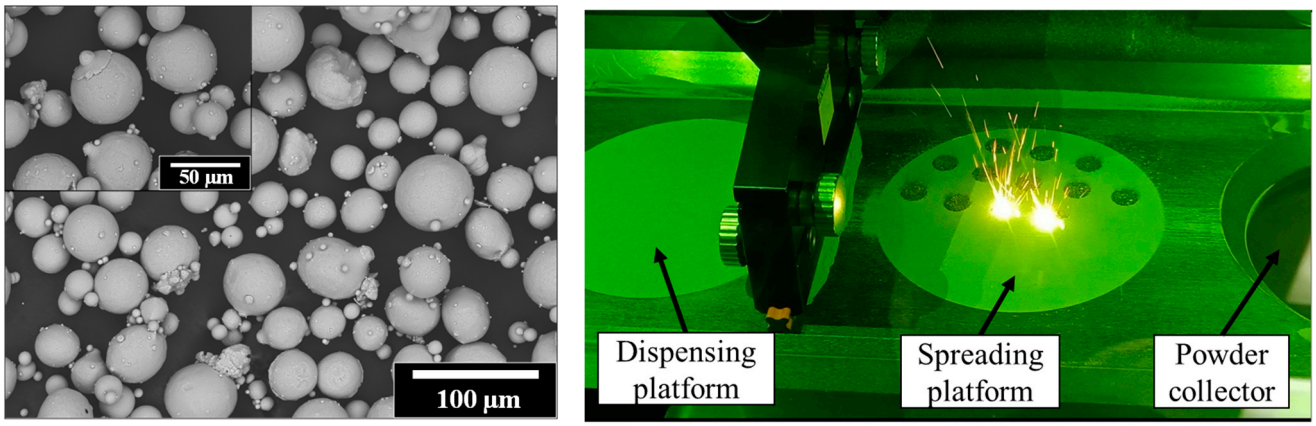

(**a**) (**b**)

Figure 1. (**a**) SEM observations of the Ti6246 powder. (**b**) Photo of the printing chamber describing the different compartments.

Table 1. Printing parameter sets used to process the Ti6246 alloy with the two layer thicknesses (t) considered.

Set	*VED* (J/mm^3)	*BR* (cm^3/h)	*t* (µm)	*h* (µm)	*h*/*t*	*P* (W)	*v* (mm/s)
I	100	5	50	150	3	139	185
II			25	75		139	741

In order to transfer the optimized printing conditions from the previous printing case (layer thickness 50 µm) to the new one (layer thickness 25 µm), the energy delivered to the powder bed (*VED*) and the build rate (*BR*) were kept constant. Next, to guarantee similar laser track overlap, and therefore continuous and stable melting conditions, the hatching distance-to-layer thickness ratio (h/t) was also maintained constant. To satisfy these conditions, dividing the layer thickness in half was compensated by a four-fold increase in the scanning speed v, from 185 to 741 mm/s (Set II in Table 1).

Firstly, two types of bulk specimens were printed: dense cubic specimens with single laser tracks on their top surface (Figure 2a) and 10 mm-diameter, 21 mm-height cylindrical specimens (Figure 2b). The cubic specimens were removed from the baseplate and used for single track width measurements with the second objective of evaluating the quality of single tracks and improving the printing accuracy via the adjustment of a laser beam offset. The cylindrical specimens were removed from the baseplate, their supports were cut off, and the remaining parts partitioned to obtain samples for porosity and structural analyses and compression testing (Figure 2b). In addition, to assess the printability limits, wall (Figure 2c) and gap (Figure 2d) design artefacts with widths ranging from 0.1 to 2 mm were printed (see Figure 2e,f).

To provide an example of a more complex part, the pressure drop measurement artefacts containing eight 60°-oriented hollow channels were also printed (Figure 3a). Channels 1 to 7 were identical (A = 0.86 mm^2), while Channel 8 was larger (A = 1.11 mm^2), but contained a narrower part (A = 0.13 mm^2) at one of its extremities (Figure 3b,c). Images of the printed pressure drop artefacts are shown in Figure 3d.

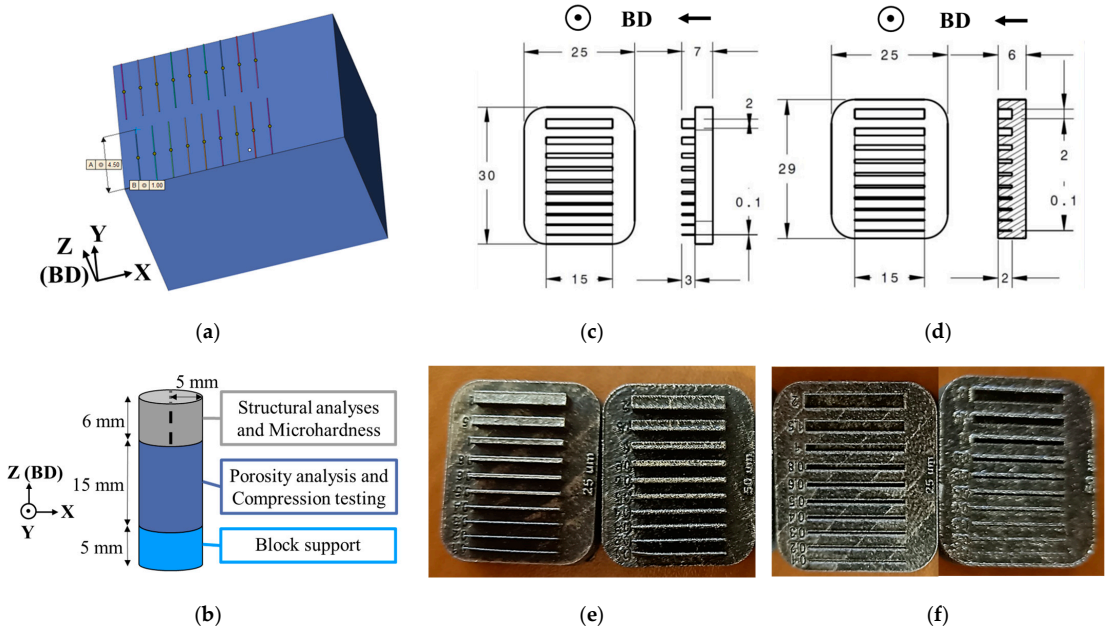

Figure 2. Schematic representation of the (**a**) cubic specimen with single tracks printed on its upper surface; (**b**) cylindrical specimen with samples used for various analyses. Drawings of the printed geometric artefacts: (**c**) walls and (**d**) gaps. Printed artefacts using 25 and 50 µm layer thicknesses: (**e**) walls and (**f**) gaps. All dimensions are in millimeters (mm). BD stands for "Build Direction".

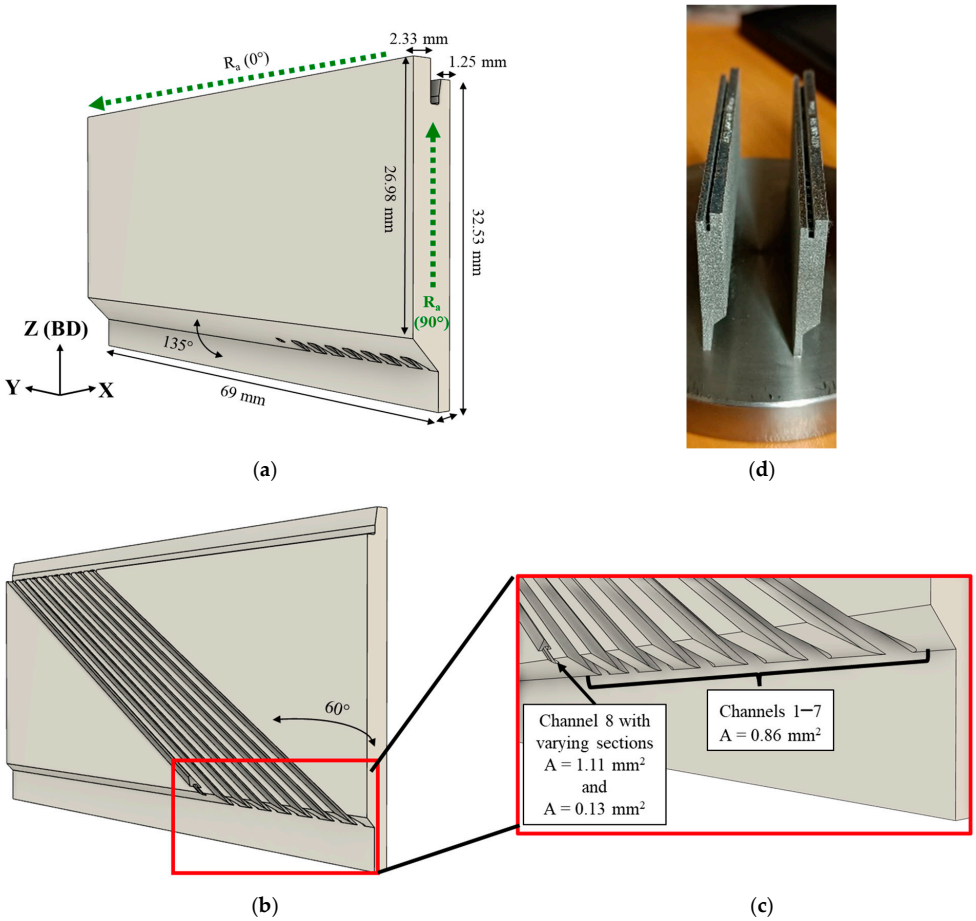

Figure 3. Schematic representation of the pressure drop artefacts: (**a**) full view, (**b**) cut view to observe the channels and (**c**) zoomed view at the channels extremity; (**d**) printed pressure drop artefacts. Green dotted lines on full view highlight the surfaces for roughness measurement.

All the parts of the study were printed using both layer thicknesses, i.e., 50 and 25 µm. No specific printing strategy was used for the cylindrical specimens, where the layers were melted using zigzag scan patterns with a ±51° rotation between them. Conversely, to improve the geometric conformity of the wall, gap and pressure drop artefacts, they were contoured using the same printing parameters as for core printing with an offset obtained from single track measurements. No specific down-skin strategy was used to print channel-containing parts. All steps related to print preparation (including slicing) were carried out using Magics (Materialise, v25.01) software.

2.2. Specimen Characterization

2.2.1. Single Tracks and Printed Density

Single tracks produced on the dense cubic specimens (Figure 2a) were analyzed using a Keyence optical VHX7000 microscope (Osaka, Japan). Their average width was extracted from ten equally-distanced height profile lines traced perpendicular to the tracks. To obtain printed density information, micro-computed tomography (µCT) scans were realized on 15 mm long middle parts of the cylindrical specimens (volume analyzed ≈ 1000 mm^3). The scans were acquired using an FF35 CT system (Comet Yxlon, Hamburg, Germany), with the following acquisition parameters: tube voltage of 140 kV, tube current of 50 µA, 1500 projections, exposure time of 475 ms over 3 frames integration and a 0.3 mm-thick copper filter for beam hardening correction. The projections were corrected and reconstructed using Siemens CERA software (v2402.9.0), resulting in a voxel size of 8 µm. Porosity analyses were carried out using Dragonfly 3D World software (v2024.1, COMET technologies, Montreal, QC, Canada) with manual thresholding for segmentation. A 6-connected component (faces) criterion was used to isolate each pore, and pores smaller than 3 × 3 × 3 voxels (<1.4 × 10^{-5} μm^3) were withdrawn from the dataset.

2.2.2. Microstructure

Upper 6 mm-long parts of the cylindrical specimens (Figure 2b) were cut along the building direction, mounted in carbon-doped resin, grounded with SiC abrasive paper, polished using diamond suspensions and a colloidal silica + H_2O_2 suspension and subjected to microstructural analysis. An X'Pert3 (Malvern Panalytical Ltd., Malvern, UK) diffractometer (XRD) was used to perform the phase identification. Acquisitions were made with a cobalt source (Kα Co = 1.79026 Å) operated at 45 kV and 40 mA, in the Bragg–Brentano configuration, with a step size of 0.017° and a 20–90° 2θ range. The microstructural state was confirmed by metallographic analysis using chemical etching with a Kroll reagent (93% H_2O, 5% HNO_3, 2 HF) of the polished cross-sections. The prepared surfaces were then observed with a LEXT OLS4100 (Lext Olympus Corp., Tokyo, Japan) confocal microscope and with a SU-8230 Field Emission STEM (Hitachi, Tokyo, Japan) scanning electron microscope.

2.2.3. Mechanical Properties

Microhardness measurements were performed on the etched Y-Z cross-sections of 6 mm-long upper parts of the cylindrical specimens using a Struers Duramin-40 M1 microhardness tester (Ballerup, Denmark). For each specimen, 10 measurements were carried out in the middle of the samples with an applied force of 300 gF and a dwell time of 15 s. After the as-printed density measurements, room-temperature compression tests were realized on 15 mm-long middle parts of the cylindrical specimens using an Alliance RF/200 testing machine (MTS, Eden Prairie, MN, USA) according to the E9-09 ASTM standard [37]. The compression rate was set at 0.01 mm/s, and the force and the displacements was measured using a 200 kN MTS load cell and an LVDT, respectively. The following metrics were extracted from the measurements: the Ultimate Compression Strength (UCS, MPa), defined

as the maximum stress reached during the test; the Yield Strength (YS, MPa), calculated by moving the slope from the origin to 0.2% on the strain axis, and the elongation to failure (δ, %).

2.2.4. Surface Roughness Measurements

The surface roughness measurements were performed using a Mitutoyo SJ410 profilometer (Mitutoyo, Kawasaki, Japan), following the ISO 21920-2 [38] standard (R profile, λs = 8 µm, 5 repetitions with a cut-off at 2.5 mm and a Gauss filter) on the upper and lateral sides of the pressure drop artefacts, respectively, at 0 and 90° (Figure 3a) with respect to the building direction.

2.2.5. Geometric Analysis

To assess the geometric compliance of the printed parts relative to their CAD drawings, high quality µCT scans of each artefact were realized using the same equipment described in Section 2.2.1. Due to the difference in dimensions between the wall/gap and channeled artefacts, the acquisition parameters were adapted from one artefact to another. The voltage and the current of the X-ray tube were set to 175 kV and 140 µA, and the copper filter used to harden the histogram was 0.5 mm thick. For each of the artefacts, 3000 projections were acquired. The walls and gaps were obtained with a 0.714 ms exposure time, while for the channeled parts, it was increased to 0.909 ms due to their larger dimensions. Overall, each projection was integrated over 3 frames for noise reduction. Siemens CERA software was used to correct the beam hardening and reconstruct the 3D volumes, leading to a final voxel size of 15 µm and 30 µm for the wall/gap and channeled artefacts, respectively.

The Dragonfly 3D World software visualization tools and Python libraries v3.12.7 (scikit-image v0.25.0, OpenCV v4.10.0, etc.) were used for the artefacts' inspection and image processing. For the wall artefacts, the wall thickness was measured for each of the 200 2D XY sections (15 µm-spaced) extracted from the 3D reconstructed volumes. For each section, the feature edges were segmented using a Sobel filter, Otsu thresholding and profile line averaging along the length of the artefact. For the gap artefacts, the gap width was calculated for each of the 133 2D XY slices (15 µm-spaced) by dividing the surface of the gap by its length. Note that the surface of each gap corresponded to a sum of pixels (15×15 µm^2) encompassed between its segmented edges. In addition, Dragonfly software was used to calculate the true volumes of each feature (walls and gaps) and to compare them with their nominal CAD values.

The channels conformity was analyzed by segmenting their 2D XZ cross-sections. Note that these 2D cross-sections were computed only in the middle part of the channels. Indeed, the channels are rectangular and oriented; therefore, their areas in such 2D section vary at extremities. In the XZ 2D view, channels 1 to 7 have a nominal cross-section area equal to 0.99 mm^2, while the widest section of channel 8 has a nominal area value of 1.28 mm^2. The variation of the thinnest section of channel 8 was not segmented due to technical limitations. Indeed, with such poor resolution (voxel size = 30 µm), this narrow channel (width = 400 µm) corresponds to only 13 voxels, compromising the segmentation.

Next, the CT volumes of each of the artefacts (walls, gaps and channels) were segmented, converted into a mesh and registered with their nominal equivalents. The iterative closest point algorithm implemented in the software was used to register one mesh with another using the best fit approach. A signed deviation map was generated and the cumulative statistical deviation of each artefact was calculated.

3. Results and Discussions

3.1. Printability and Properties of Printed Part

3.1.1. Visual Aspect of Printing

For the two parameter sets of the study, the visual aspect of printing jobs differed. Set I with thicker layers generated much more sparkles during printing and much more residual spatters on the build chamber walls after printing. This is in agreement with the observations by Pauzon et al. in their study on Ti64 LPBF printability [39], where increasing the layer thickness increased the quantity of spatters per scanned layer. In the present study, this effect was compounded by a four times slower scanning speed for Set I as compared to Set II: 185 mm/s for Set I versus 741 mm/s for Set II. Due to this slower scanning, the linear energy density $LED = P/v$ for Set I was four times higher than for Set II (0.75 J/mm versus 0.19 J/mm), theoretically making the vapor plume above the melt pool less stable, promoting the ejection of droplets [40] and potentially influencing the final print quality.

3.1.2. Physical and Mechanical Properties of Printed Specimens

Both printing parameter sets led to overall continuous and homogeneous tracks (Figure 4). However, due to a decrease in the scanning speed, the single track (melt pool) width (W) generated by Set I (t = 50 µm) was almost twice that generated by Set II (t = 25 µm): 297 ± 11 µm versus 145 ± 12 µm (Figure 4a,b). The single track width values are reported in Table 2. Note that regular rippled patterns were observed on the surface of single tracks printed with Set I, while Set II promoted the formation of some humps along the tracks. According to the literature [41,42], these features are consistent with the parameters used. Using lower linear energies with higher scanning speeds (Set II) promotes hump formation caused by the periodic separation of melt pools and solidification shrinkage, while higher linear energies with lower scanning speeds increase melt pool thermal instability and promote excessive heat accumulation, with strong recoil pressure pushing back the molten metal and inducing the formation of ripples. Overall, due to the lower scanning speed, which means the laser dwells longer in a given location, single tracks printed with Set I appear more uniform, with less unmelted particles stuck along, but with more spatters solidified around. Despite the difference in terms of melt pool physics, both parameter sets enabled printing high-density parts, systematically denser than 99.98%, with only a limited number of small highly spherical pores observed (Figure 4c,d). Note also that in both cases, a certain number of partially-melted particles were stuck to the printed parts.

Figure 5a shows the results of the XRD analysis and highlights the formation of the orthorhombic α'' martensitic phase. For both cases, the confocal microscope observations revealed homogeneous microstructures with partially visible melt pool borders and typical columnar prior-β grains. Moreover, the higher magnification SEM observations shown in Figure 5b,c revealed a less than 2% difference in size of martensite needles, arranged in a cross-hatch pattern for both sets of parameters used (Table 2). This microstructure similarity is caused by the almost identical W/h ratio for two cases, leading to the same relative overlap R% (3) of two neighboring tracks. Thus, even though the single track width for Set I was significantly larger that for Set II, this difference was compensated by a much larger hatching space for Set I than for Set II, thus enabling the formation of identical microstructures. The calculated R% values for the two sets of parameters are presented in Table 2.

$$R\% = \frac{W - h}{W} \times 100 \quad (3)$$

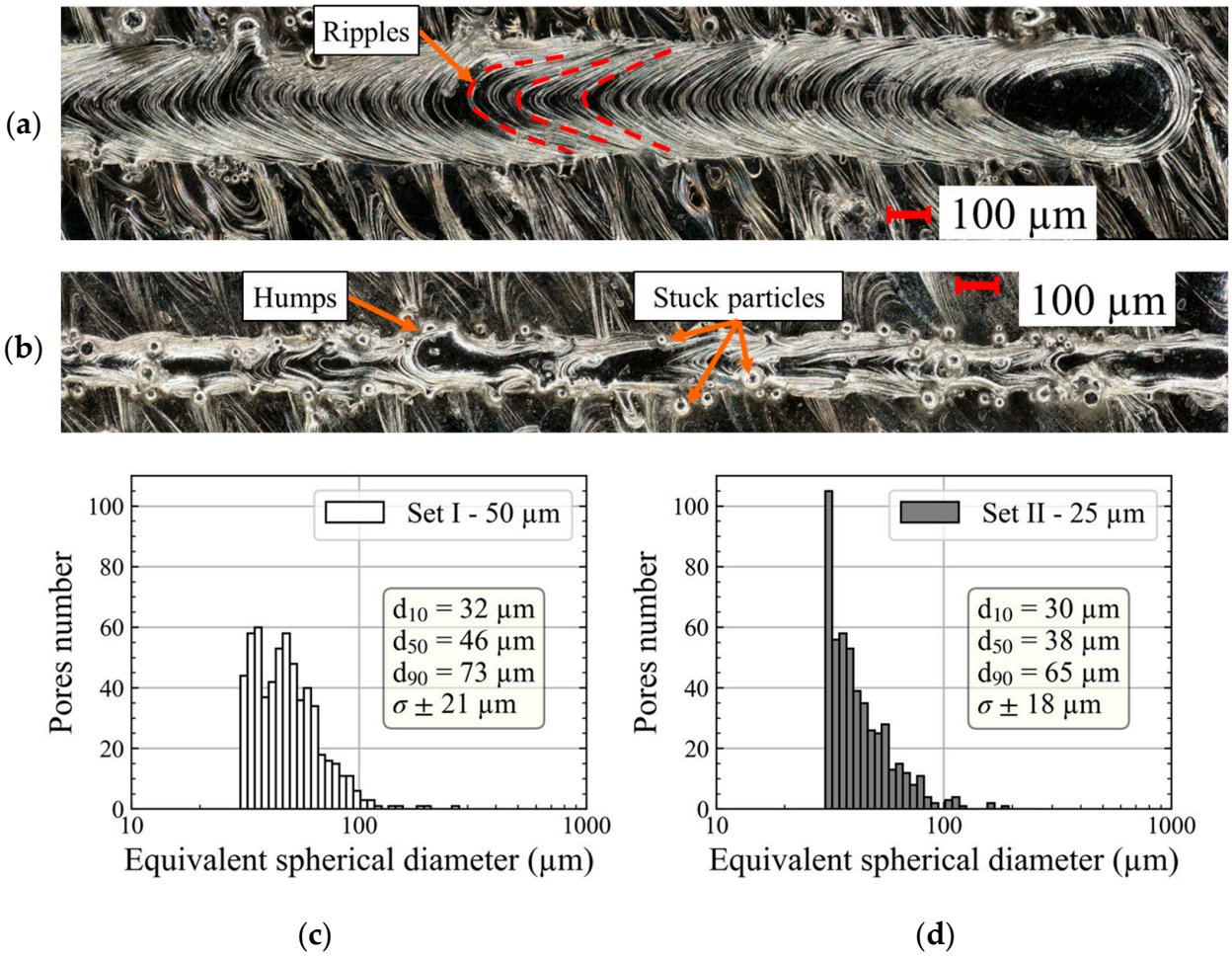

Figure 4. Optical observations of the continuous single tracks printed using (**a**) Set I and (**b**) Set II. Equivalent pore diameter distributions corresponding to a volume of 1 cm^3: (**c**) Set I—50 µm, (**d**) Set II—25 µm; (cylindrical specimens).

Table 2. Physical and mechanical properties of the as-built samples printed using two different layer thicknesses (*t*).

Set	Single Track Width (*W*) (µm)	α″ Needle Width (nm)	*W*/*h*	*R*% (%)	Microhardness HV0.3	YS (MPa)	UCS (MPa)	δ (%)
I (50 µm)	297 ± 11	48 ± 11	2.0	49	447 ± 37	1075 ± 65	1115 ± 65	7 ± 0.4
II (25 µm)	145 ± 12	49 ± 17	1.9	48	471 ± 26	1045 ± 29	1120 ± 33	7 ± 1

Finally, the two parameter sets led to the very close as-built mechanical properties summarized in Table 2, which is not surprising, given their structural similarities (α″ needle sizes and patterns). Regardless of the layer thickness used, the printed parts exhibited the same microhardness values, failed in a similar stress range (>1000 MPa) and were relatively brittle (δ < 9%). It can therefore be confirmed that holding constant (a) the volumetric energy density *VED*, (b) the building rate *BR* and (c) the hatching space-to-layer thickness ratio (*h*/*t*) allowed keeping the as-built Ti6246 alloy's physical and mechanical properties almost identical, despite the use of significantly different layer thicknesses.

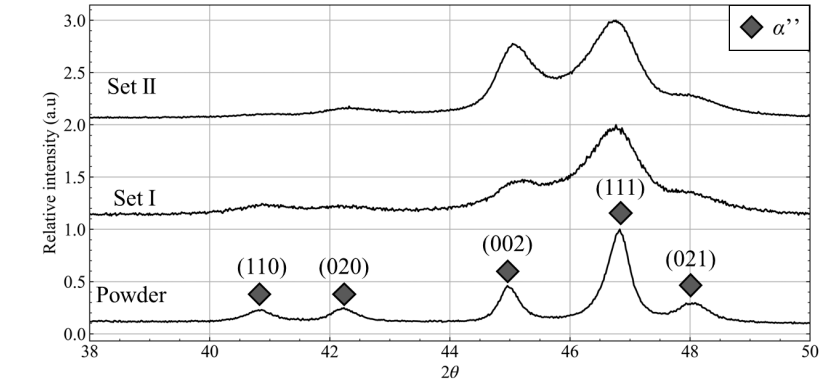

(**a**)

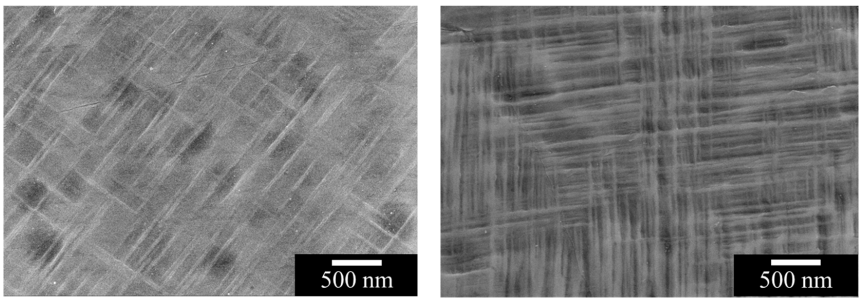

(**b**) (**c**)

Figure 5. (**a**) XRD diffractograms of the Ti6246 powder and of the as-built samples printed with both parameter sets; SEM images with the α'' martensite needles in samples printed with (**b**) Set I and (**c**) Set II.

3.2. Surface Roughness and Geometric Compliance

3.2.1. Surface Roughness

For each of the two layer thicknesses, the Ra values measured for the 0° (top) and 90° (lateral) oriented surfaces of the pressure drop artefacts are summarized in Figure 6. As commonly observed [43,44], the lateral surfaces were significantly rougher than the top surfaces. Moreover, for both surface orientations, the surface roughness of Set I artefacts (t = 50 µm) was significantly higher than that of their Set II counterparts (t = 25 µm), where thicker layers caused (a) a greater propensity to ripple formation on the top surfaces (see Section 3.1.2 for explanation) and (b) a larger distance between layers on the lateral surfaces.

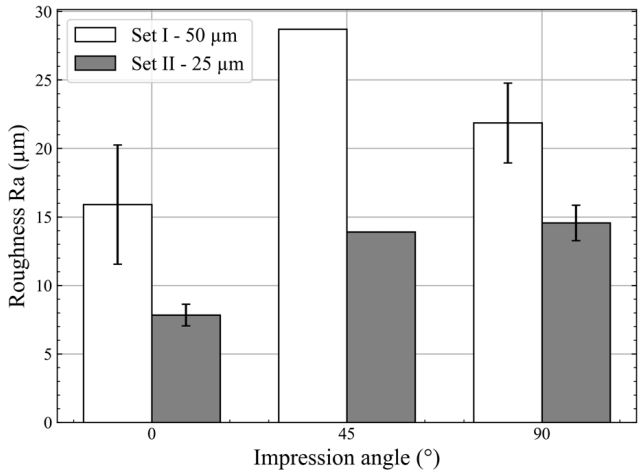

Figure 6. Surface roughness (Ra) measured on the pressure drop artefact as a function of the build angle for both parameter sets. Impression angles 0° and 90° were obtained on the top and lateral surfaces of the artefact.

3.2.2. Conformity of Walls and Gaps

The geometric compliance of the wall and gap artefacts was evaluated along the build direction, and a summary of the average size of each feature is reported in Figure 7a, for wall thicknesses, and in Figure 7b, for gap widths. Note that for both cases, no significant variations of the wall thickness and gap width along the build direction were observed.

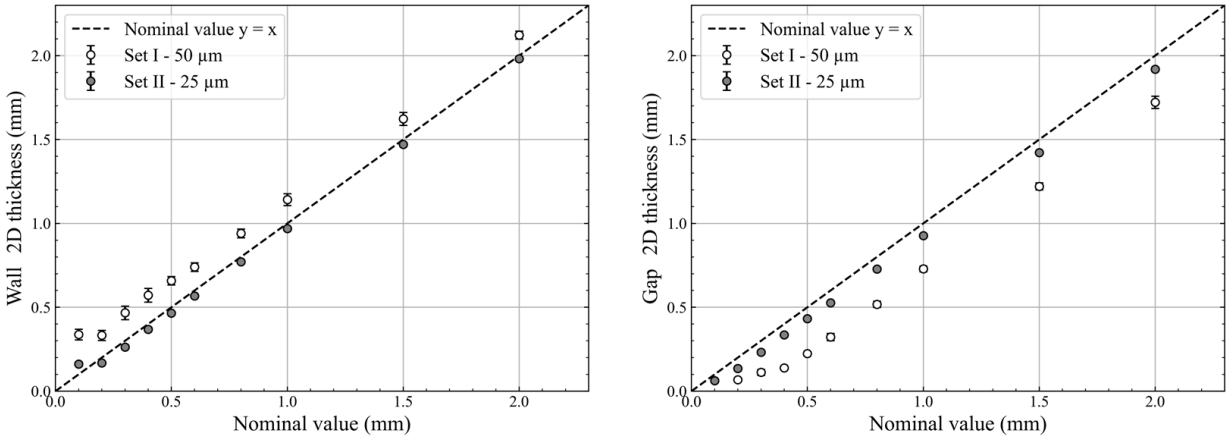

(**a**) (**b**)

Figure 7. Average (**a**) wall thickness and (**b**) gap width for Sets I and II artefacts printing after segmentation of the µCT 2D XY sections; error bars are smaller than the markers.

The 0.1 and 0.2 mm-thick wall/gap features must be considered on their own merits, as they represent exceptional cases that fall within the range of single track widths, being formed by only one laser path (Table 2). In the case of wall artefacts, these two features had the same average thicknesses. However, the difference with the nominal values is greater for Set I than for Set II because of the wider melt pools (single tracks) in the former case (Figure 7a). Note that the wall thicknesses reported here are slightly larger than those reported for single tracks in Section 3.1.2 ($\Delta W \approx$ 20–30 µm) due to the thermal history of the powder bed, which can vary between the prints (e.g., the number of parts on the build plate, the printing parameters used for surrounding parts, etc.). According to these observations, the thinnest printable wall thickness corresponds roughly to the single track width, i.e., 0.3 mm for Set I and 0.15 mm for Set II (Figure 7a). Given the substantial width of melt pools (single tracks) for Set I, gaps with a nominal width smaller than 0.2 mm were almost fully clogged, but they were printable with Set II (Figure 7b). For both layer thicknesses, the gaps were narrower than their nominal values, due to particles partially-melted to their edges, with these deviations being systematically greater for Set I artefacts as compared to their Set II equivalents. This behavior is consistent with the single track analyses (Figure 4a,b).

The 3D volume segmentation of each of the two features (Figure 8) allowed comparisons with the nominal volumes. Overall, the measurement performed on features printed using Set II (t = 25 µm) are in line with the nominal values, except for the thinnest features (0.1 mm) in which case deviations are observed, mainly because single tracks are wider that the desired feature. Conversely, a significant shift in the volume values is reported for features printed with Set I (t = 50 µm). For features with nominal values smaller than 1 mm, a rapid decline in the geometric compliance is observed. These observations are consistent with the melt pool (single track) measurements (see Sections 3.1.1 and 3.1.2). Wider melt pools and more sparks associated with Set I promoted the sticking of unmelted particles or solidified spatters to the outer contours of the printed part. Therefore, using Set II with thinner layers allowed accurate (5% deviation) printing of features larger than 0.2 mm, while Set I induces notable deviations (>20%) for features smaller than 1.0 mm.

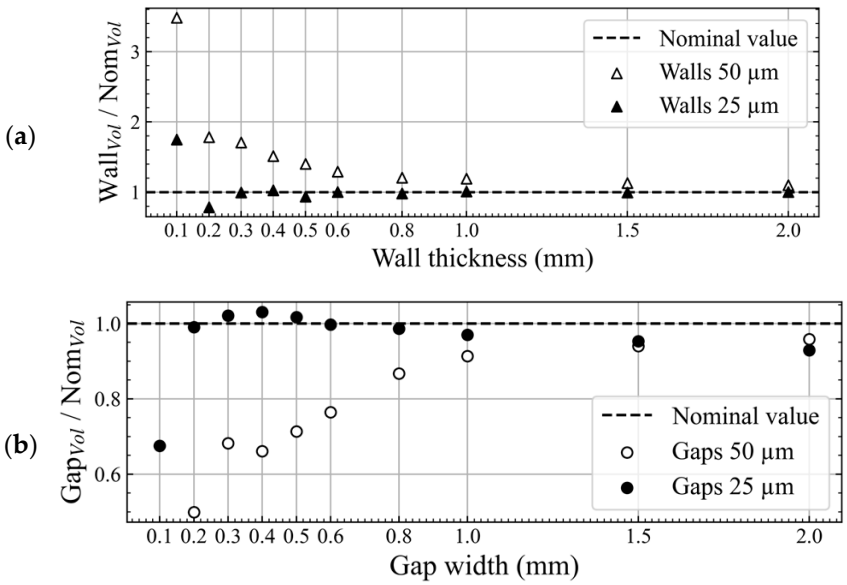

Figure 8. Evolution of the segmented 3D volume compared to the nominal volume for both parameter sets for (**a**) walls and (**b**) gaps. In each figure, black dashed lines correspond to the nominal thickness of features.

The entire deviation analysis of the wall and gap artefacts was completed using the computation of signed distance maps (Figure 9). Note that the significant deviations reported in both cases for the 0.1 mm-thick walls are related to their fragility and accidental deformations occurring during the sample removal from the baseplate. Overall, the colored deviation maps illustrate the major difference in printing accuracy between the two parameter sets. As mentioned in Section 3.1.2, Set I (Figure 9a), with the highest *LED*, was correlated with ripples and a large number of undesired spatters solidified on the top surface, generating some significant deviations. Conversely, the top surfaces that were printed with Set II (Figure 9b) had a much better geometric compliance, with deviations close to the particle size range (≈60 µm).

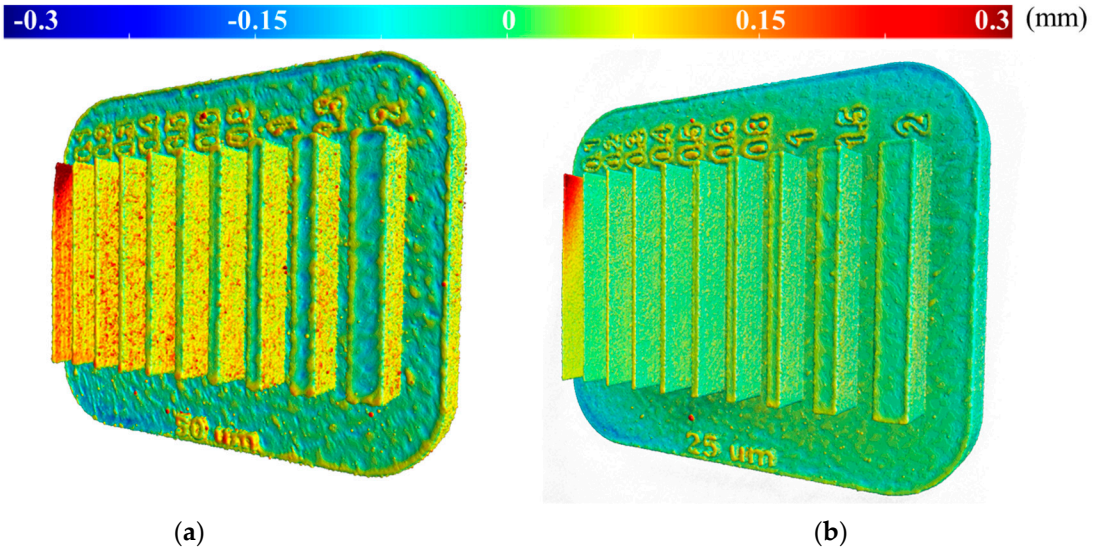

(**a**) (**b**)

Figure 9. A 3D visualization of the deviation map compared to the CAD for walls printed with (**a**) Set I (t = 50 µm), (**b**) Set II (t = 25 µm).

Regarding the lateral faces (90°), significant deviations (>100 µm) were systematically reported with Set I (Figure 9a), suggesting that these surfaces were more prone to attracting

a lot of particles and solidified spatters surrounding the melt pool. This behavior is attributed to the higher *LED* brought to the powder bed, which increases the melt pool size and average temperatures [45], decreases the viscosity of molten metal and, finally, promotes the sticking of particles from the powder bed. In addition, the low scanning speed induces heat accumulation, which influences the melt pool physics (e.g., Marangoni effect) and promotes overflow melting and therefore geometric deviations compared to the CAD [46]. In comparison, the lateral faces of the 3D reconstructed volume of the wall artefacts printed using Set II were almost exempt of spatters and stuck particles and had smaller deviations (Figure 9b).

Figure 10 represent the statistical distribution of the deviations computed inside the map used for 3D rendering. Overall, the distributions obtained for walls and gaps printed with Set II were narrower, with lower standard deviations and a median value centered around 0 mm (Figure 10b,d). Conversely, due to the aforementioned reasons regarding the melt pool continuity, the specimens printed with Set I had larger standard deviations and shifted median values (Figure 10a,c).

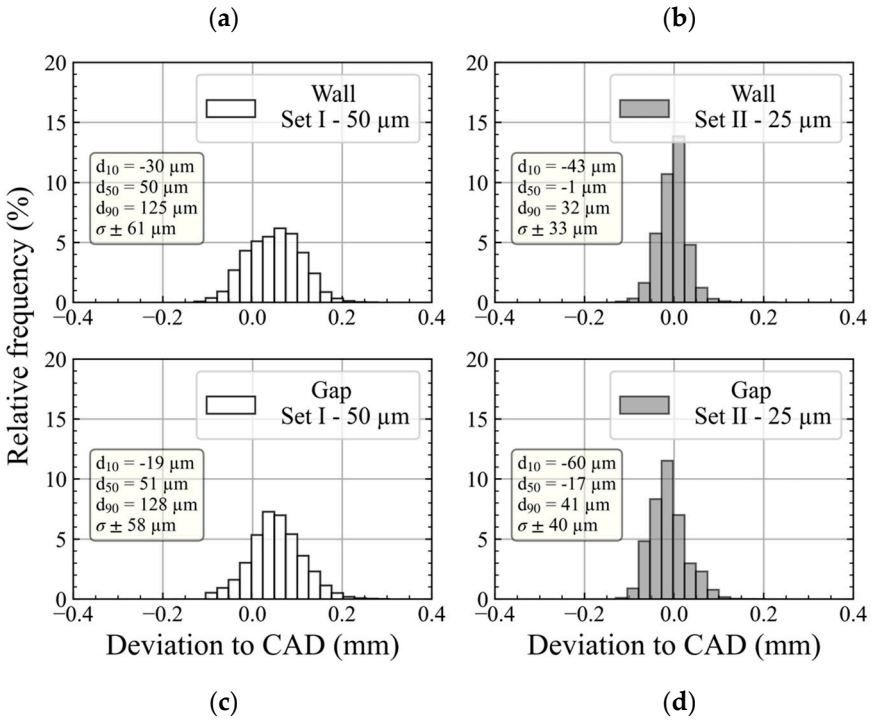

Figure 10. Three-dimensional deviation distribution for the geometric artefacts: (**a**) walls Set I (t = 50 µm), (**b**) walls Set II (t = 25 µm), (**c**) gaps Set I (t = 50 µm), (**d**) gaps Set II (t = 25 µm).

3.2.3. Conformity of the Internal Channels

Similar to the wall and gap artefacts, the pressure drop artefacts printed with both parameter sets were µCT-scanned to assess their geometrical compliance. Due to the channel orientation with respect to the building direction (60°), some stair and down-skin effects were expected. With the CAD registered on the µCT scan, these phenomena were observed in the 2D XZ sections (Figure 11a), with the partially collapsed upper edges. Each XZ slice along the length of the artefact (Y axis) was segmented (Figure 11b), and the cross-sectional areas of each channel were extracted for comparison with the nominal values.

The results indicate that, regardless of the parameter sets used, the printed cross-sectional areas are much narrower than their CAD-specified values (Figure 12a,b). The following deviations were observed for the wider channel (8): A = 0.77 mm^2 (ΔA $\approx$ 40%) for Set I and A = 0.92 mm^2 (ΔA $\approx$ 29%) for Set II. For channels 1 to 7, the considered

values correspond to the average of the values measured on each channel. Note that for the specimens printed with Set I, a significant variation was observed between the area values measured on each channel, while for the specimens printed with Set II, the channels were more uniform, and the area values were less dispersed ($\sigma_{A\ Set\ I} \approx 3\sigma_{A\ Set\ II}$). Overall, for Set I, the average area value was A = 0.62 mm^2 ($\Delta A \approx 37\%$), and for Set II A = 0.71 mm^2 ($\Delta A \approx 28\%$). The difference in dimensions between Channels 1–7 and Channel 8 does not impact the conformity of printed cross-section area values with their nominal equivalents. Indeed, the same shape factor (A_{Exp}/A_{Nom}) was obtained for all the channels: 0.6 for Set I (thicker layers) and 0.7 for Set II (thinner layers). Similar to the wall/gap artefacts discussed in Section 3.2.2, the distributions shown in Figure 12c (Set I) and Figure 12d (Set II) highlighted a significant difference in geometrical compliance between the parameter sets. Using thinner layers (t) enabled improving the geometric compliance, with reduced standard deviation values.

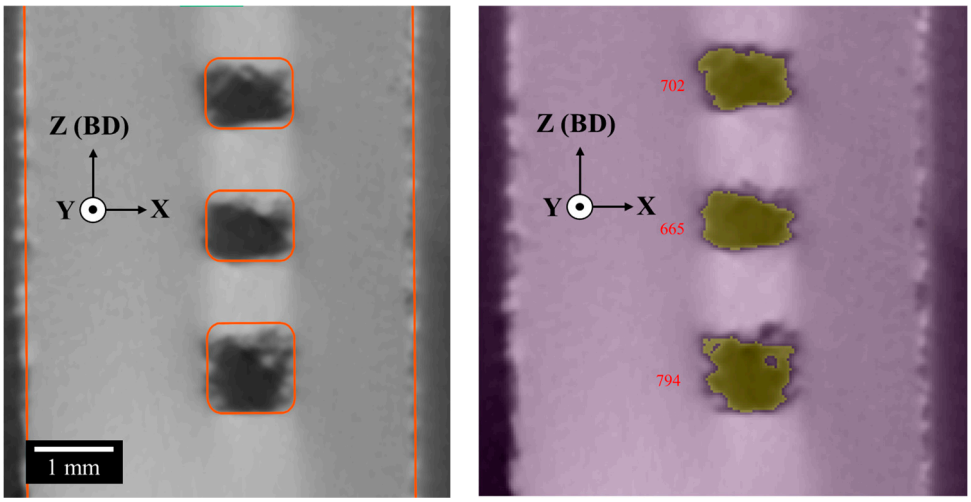

(**a**) (**b**)

Figure 11. (**a**) Overlapping of the µCT scan (Set I) and the CAD mesh (orange line) after registration in the 2D XZ section to highlight the down-skin effect on the upper surface of the channels. (**b**) Segmented (yellow) 2D XZ slice with the cross-sectional areas measured after segmentation.

The geometric compliance analysis conducted on the pressure drop artefacts also highlighted the fact that an excessive roughness resulting from the thicker layers (Set I) (see Section 3.2.1) can be detrimental to the printability of such a complex channeled geometry. Indeed, it was observed that the reduced section of this specific channel (n°8) was partially clogged due to its internal roughness and the particles stuck to its surfaces (Figure 13a). In comparison, Figure 13b shows that the same thin section has a greater geometrical compliance to CAD, when the artefact was printed with thinner layers (t = 25 µm, Set II). From the 3D views of the computed deviation maps, the flow passage in the artefact printed with Set I (Figure 13c) appears to be considerably more obstructed than for the case of Set II (Figure 13c). Overall, as expected, in printing the oriented channels, the largest deviations were systematically located at their upper partially collapsed surfaces. As far as the average channel geometric compliance is concerned, cross-sections of channels 1 to 7 printed with Set II were 13% wider than those printed with Set I, while the cross-section of channel 8 was 16% wider.

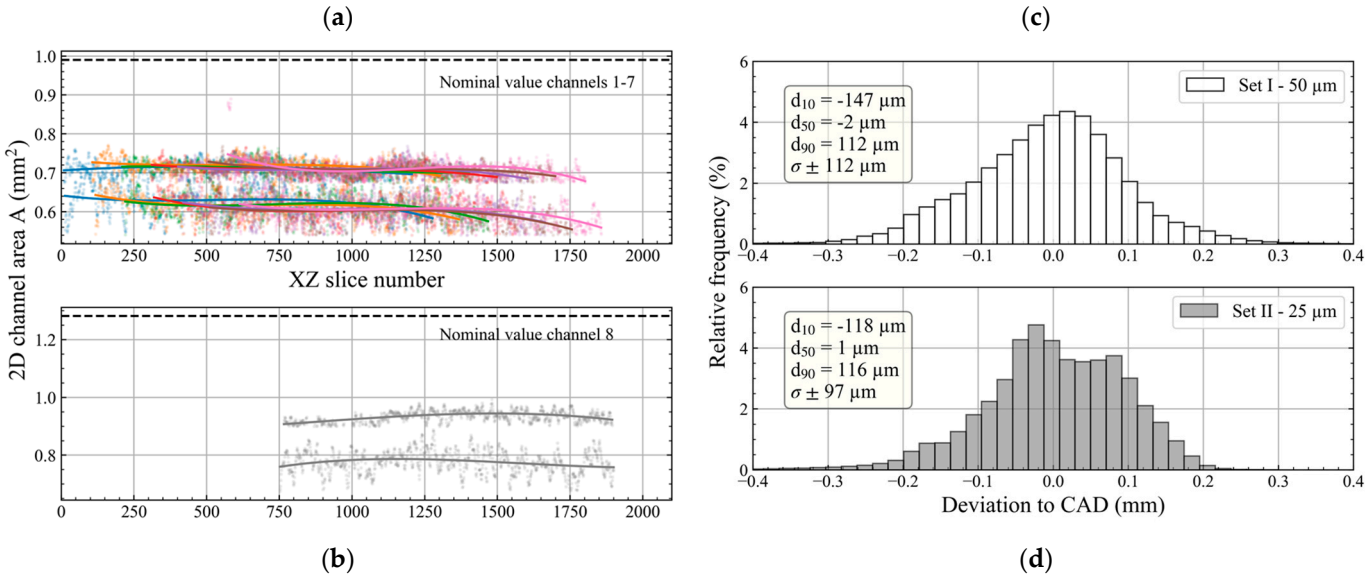

Figure 12. Evolution of the cross-section areas along the XZ direction of (**a**) channels 1 to 7, (**b**) channel 8. Deviation distribution obtained for the pressure drop specimen printed with parameter sets: (**c**) Set I, (**d**) Set II.

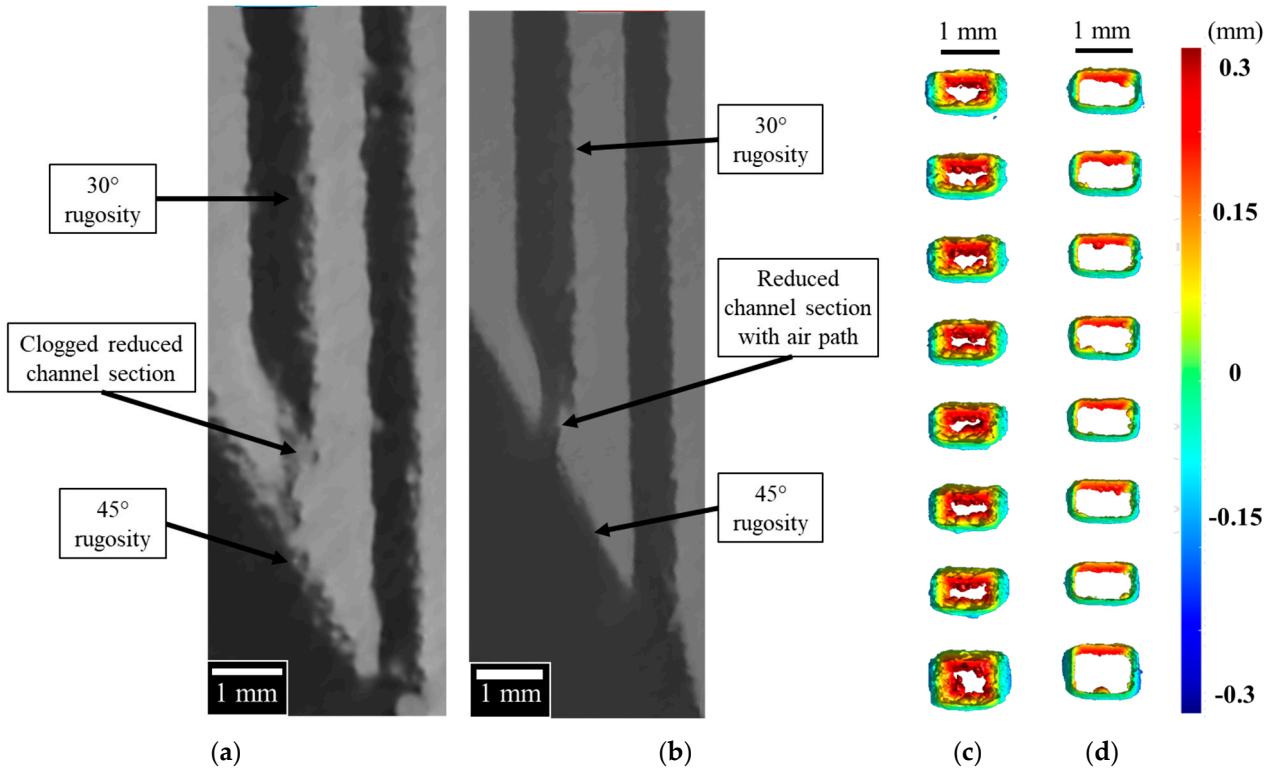

Figure 13. A 2D slice of the reduced section of the widest channel (n°8) printed with (**a**) Set I (t = 50 µm) and (**b**) Set II (t = 25 µm). The section is partially clogged using the parameter with the higher layer thickness. (**c**) A 3D view of one extremity of the deviation map computed for the height channels: (**c**) Set I (t = 50 µm), (**d**) Set II (t = 25 µm).

It is thus evident that a significant internal roughness combined with a lack of geometric compliance must have had a negative effect on the air flow inside the channel. To assess this impact, the pressure drop tests were realized with channeled artefacts printed using two different layer thicknesses. The artefacts were installed downstream of a pressure-monitored plenum with a controlled air flow ($T_{air} \approx 20$ °C) ranging from 0.5 to 6 g/s, and manifested a ~30% difference in air flow, which is twice the difference in the corresponding cross-sectional areas. In can therefore be stated that to obtain a better geometric compliance of such channel-contained parts, they should be printed with the smallest layer thickness *t* (Set II) available, albeit at the expense of process productivity.

Several technical solutions can be considered to further improve the geometric conformity of such complex parts. Some authors suggest replacing a circular shape of channels by the droplet shape to improve the channel roundness [47]. The other compensates deviations from the nominal values by adapting the CAD dimensions using the results of µCT analysis of printed parts [48,49], or optimizing the printing strategy [50].

3.3. Influence of the Layer Thickness on Process Productivity

Finally, to assess the impact of reducing the layer thickness in half, and consequently adapting the parameter selection strategy on the process productivity, a comparison was made between two builds printed with each parameter set. Two different prints were considered: Print A, consisting of 12 dense prismatic specimens (81 mm in height, 17 × 3 mm in cross-section) built on a 3 mm-thick dense support, representing a total volume of 51,408 mm^3, and Print B, including the same 12 prismatic specimens along with 8 additional cylindrical specimens, for a total volume of 67,444 mm^3. These builds were designed to take advantage of a full available height of the build chamber (84%).

Their respective production times are presented in Table 3. As expected, the recoating time for both builds approximately doubled when reducing the layer thickness, while the total build time increased by only about 25% for the thinner layers. This can be explained by the fact that recoating represents only 20–35% of the total build time. The printing parameters for Set II resulted in only a 10% longer overall laser exposure time, related to longer skywriting times in the case of narrower distances between neighbouring tracks (smaller hatching space).

Table 3. Comparison of production time required to print two different builds (Print A and Print B) using parameter Set I (*t* = 50 µm) and Set II (*t* = 25 µm).

	Print A		**Print B**	
Layer Thickness (µm)	**50 (Set I)**	**25 (Set II)**	**50 (Set I)**	**25 (Set II)**
Melting time (s)	19,183	21,290 (+10%)	24,470	26,955 (+9%)
Recoating time (s)	6562	12,988 (+49%)	6558	13,074 (+50%)
Total production time (s)	28,774	38,319 (+25%)	33,995	43,923 (+23%)

Therefore, the parameter selection approach related to the layer thickness reduction enabled improving the printing accuracy and preserving comparable physical (density, flaw–defects proportion) and mechanical properties (high YS, low δ) of printed parts at the expense of an enviable increase in incompressible recoating and skywriting times, and, therefore, in a lower process productivity.

4. Conclusions

In this study, the well-established layer thickness reduction strategy for improving the accuracy and surface roughness of LPBF parts was employed. However, to avoid the time-consuming task of re-optimizing the entire set of printing parameters, the parameter set with layer thickness reduction (Set II) was derived from the previously optimized parameter set characterized by excellent mechanical properties but high surface roughness and low geometric compliance (Set I) [32]. In addition, three process equivalence criteria were applied during the layer thickness reduction: the volumetric energy density (*VED*), the build rate (*BR*) and the hatching distance/layer thickness ratio (h/t) were maintained constant. Satisfying these conditions resulted in specimens exhibiting similar laser track overlaps, comparable microstructures and equivalent mechanical properties. Specifically, all the as-built printed specimens were highly dense (>99.9%), displayed a thin nanometric orthorhombic α'' martensite microstructure and showed similar hardness, compression resistance and elongation to failure.

These two parameter sets were then used to print design artefacts containing thin features (walls and gaps) and inclined channels (pressure drop artefacts). A critical difference was observed using the parameter set with thicker layers (Set I—t = 50 µm). This case corresponded to wider melt pools, significant amounts of ripples, spatters and partially melted particles stuck to the printed parts, creating a significant roughness and severe deviations from the nominal values (CAD). The previous printing parameter set was found unsuitable for printing thin features smaller than 1 mm in size, while the reduction of layer thickness divided by five the printability limits, going down to 0.2 mm. Furthermore, gaps or channels printed with Set I were initially partially or entirely clogged, unlike those printed considering the layer thickness reduction (Set II).

Based on the analyses performed, it was concluded that Set II (t = 25 µm) must be preferred for printing parts containing thin features with better geometric compliance and surface finish. Nonetheless, this parameter set does not provide a complete solution for the common issue of printing channel-contained parts. To improve the geometric compliance of the latter, additional measures must be taken, including the optimization of these parts' design and printing conditions. Note that despite the same build rate (*BR*) in the case of both printing parameter sets, the geometric improvements available using Set II were made at the expense of a relatively limited increase in the overall production time (≈20–25%).

Author Contributions: Conceptualization, T.M. and V.B.; data curation, T.M. and A.L.; formal analysis, T.M. and A.L.; funding acquisition, V.B.; investigation, T.M., A.L. and P.K.D.; methodology, T.M., A.L. and V.B.; software, T.M. and A.L.; project administration, V.B.; resources, V.B.; supervision, V.B.; validation, V.B.; visualization, T.M., A.L. and V.B.; writing—original draft preparation, T.M. and A.L.; writing—review and editing, V.B. All authors have read and agreed to the published version of the manuscript.

Funding: The authors acknowledge the financial support provided by CRIAQ (Consortium de Recherche et d'Innovation en Aérospatiale au Québec) in the framework of the Exploring Innovation—INNOV-R program, NSERC (Natural Sciences and Engineering Research Council of Canada) and Exonetik Turbo Inc.

Data Availability Statement: The original contributions presented in this study are included in the article. Further inquiries can be directed to the corresponding author.

Conflicts of Interest: The authors declare no conflicts of interest. The funders had no role in the design of the study; in the collection, analyses, or interpretation of data; in the writing of the manuscript; or in the decision to publish the results.

Abbreviations

The following abbreviations are used in this manuscript:

AM	Additive Manufacturing
ASTM	American Society for Testing and Materials
BR	Build Rate
CAD	Computer-Aided Design
DED	Directed Energy Deposition
EB-PBF	Electron Beam Powder Bed Fusion
ISO	International Organization for Standardization
LED	Linear Energy Density
LPBF	Laser Powder Bed Fusion
LVDT	Linear Variable Differential Transformer
PSD	Particle Size Distribution
SEM	Scanning Electron Microscopy
μCT	Micro-Computed Tomography
VED	Volumetric Energy Density
XRD	X-Ray Diffraction

References

1. Tofail, S.A.M.; Koumoulos, E.P.; Bandyopadhyay, A.; Bose, S.; O'Donoghue, L.; Charitidis, C. Additive manufacturing: Scientific and technological challenges, market uptake and opportunities. *Mater. Today* **2018**, *21*, 22–37. [CrossRef]
2. Javaid, M.; Haleem, A.; Singh, R.P.; Suman, R.; Rab, S. Role of additive manufacturing applications towards environmental sustainability. *Adv. Ind. Eng. Polym. Res.* **2021**, *4*, 312–322. [CrossRef]
3. Hegab, H.; Khanna, N.; Monib, N.; Salem, A. Design for sustainable additive manufacturing: A review. *Sustain. Mater. Technol.* **2023**, *35*, e00576. [CrossRef]
4. Gu, D.D.; Meiners, W.; Wissenbach, K.; Poprawe, R. Laser additive manufacturing of metallic components: Materials, processes and mechanisms. *Int. Mater. Rev.* **2012**, *57*, 133–164. [CrossRef]
5. Sanchez, S.; Smith, P.; Xu, Z.; Gaspard, G.; Hyde, C.J.; Wits, W.W.; Ashcroft, I.A.; Chen, H.; Clare, A.T. Powder Bed Fusion of nickel-based superalloys: A review. *Int. J. Mach. Tools Manuf.* **2021**, *165*, 103729. [CrossRef]
6. Rometsch, P.A.; Zhu, Y.; Wu, X.; Huang, A. Review of high-strength aluminium alloys for additive manufacturing by laser powder bed fusion. *Mater. Des.* **2022**, *219*, 110779. [CrossRef]
7. Narasimharaju, S.R.; Zeng, W.; See, T.L.; Zhu, Z.; Scott, P.; Jiang, X.; Lou, S. A comprehensive review on laser powder bed fusion of steels: Processing, microstructure, defects and control methods, mechanical properties, current challenges and future trends. *J. Manuf. Process.* **2022**, *75*, 375–414. [CrossRef]
8. Colombo-Pulgarín, J.C.; Biffi, C.A.; Vedani, M.; Celentano, D.; Sánchez-Egea, A.; Boccardo, A.D.; Ponthot, J.-P. Beta Titanium Alloys Processed by Laser Powder Bed Fusion: A Review. *J. Mater. Eng. Perform.* **2021**, *30*, 6365–6388. [CrossRef]
9. Stopyra, W.; Gruber, K.; Smolina, I.; Kurzynowski, T.; Kuźnicka, B. Laser powder bed fusion of AA7075 alloy: Influence of process parameters on porosity and hot cracking. *Addit. Manuf.* **2020**, *35*, 101270. [CrossRef]
10. Sabzi, H.E.; Maeng, S.; Liang, X.; Simonelli, M.; Aboulkhair, N.T.; Rivera-Díaz-del-Castillo, P.E.J. Controlling crack formation and porosity in laser powder bed fusion: Alloy design and process optimisation. *Addit. Manuf.* **2020**, *34*, 101360. [CrossRef]
11. Ayers, N.; Lucas, C.; Mahmud, A.; Kljestan, N.; Knezevic, M.; Sohn, Y. Parameter Optimization and Flaw Type Dependent Tensile Properties of 15-5PH Stainless Steel Manufactured by Laser Powder Bed Fusion. *Adv. Eng. Mater.* **2024**, *26*, 2401346. [CrossRef]
12. Liu, B.; Zhang, P.; Yan, H.; Lu, Q.; Shi, H.; Liu, Z.; Wu, D.; Sun, T.; Li, R.; Wang, Q. A Review on Manufacturing Pure Refractory Metals by Selective Laser Melting. *J. Mater. Eng. Perform.* **2024**, *33*, 9945–9975. [CrossRef]
13. Kranz, J.; Herzog, D.; Emmelmann, C. Design guidelines for laser additive manufacturing of lightweight structures in TiAl6V4. *J. Laser Appl.* **2014**, *27*, S14001. [CrossRef]
14. Ceccanti, F.; Giorgetti, A.; Arcidiacono, G.; Citti, P. Laser Powder Bed Fusion: A Review on the Design Constraints. *IOP Conf. Ser. Mater. Sci. Eng.* **2021**, *1038*, 012065. [CrossRef]
15. Viale, V.; Stavridis, J.; Salmi, A.; Bondioli, F.; Saboori, A. Optimisation of downskin parameters to produce metallic parts via laser powder bed fusion process: An overview. *Int. J. Adv. Manuf. Technol.* **2022**, *123*, 2159–2182. [CrossRef]
16. Valiyakath Vadakkan Habeeb, N.; Islam, R.; Chou, K. Influence of Pre- and Post-Contouring Strategies to Downskin Sloped Surfaces in Laser Powder-Bed Fusion (L-PBF) Additive Manufacturing. *Materials* **2024**, *17*, 2639. [CrossRef]

17. Calignano, F.; Cattano, G.; Manfredi, D. Manufacturing of thin wall structures in AlSi10Mg alloy by laser powder bed fusion through process parameters. *J. Mater. Process. Technol.* **2018**, *255*, 773–783. [CrossRef]
18. Gaikwad, A.; Imani, F.; Yang, H.; Reutzel, E.; Rao, P. In Situ Monitoring of Thin-Wall Build Quality in Laser Powder Bed Fusion Using Deep Learning. *Smart Sustain. Manuf. Syst.* **2019**, *3*, 98–121. [CrossRef]
19. Kushwaha, A.; Subramaniyan, A.K.; Bommanahalli Kenchappa, N.; Barad, S. Microstructure, mechanical, and wear properties of thin-walled Ti6Al4V parts produced using laser powder bed fusion technique. *Mater. Lett.* **2022**, *308*, 131138. [CrossRef]
20. Baier, M.; Sinico, M.; Witvrouw, A.; Dewulf, W.; Carmignato, S. A novel tomographic characterisation approach for sag and dross defects in metal additively manufactured channels. *Addit. Manuf.* **2021**, *39*, 101892. [CrossRef]
21. Charles, A.; Bayat, M.; Elkaseer, A.; Thijs, L.; Hattel, J.H.; Scholz, S. Elucidation of dross formation in laser powder bed fusion at down-facing surfaces: Phenomenon-oriented multiphysics simulation and experimental validation. *Addit. Manuf.* **2022**, *50*, 102551. [CrossRef]
22. Boyer, R.; Welsch, G.; Collings, E.W. (Eds.) *Materials Properties Handbook: Titanium Alloys*, 4th ed.; ASM International: Materials Park, OH, USA, 2007; ISBN 978-0-87170-481-8.
23. Yang, X.; Ma, W.; Zhang, Z.; Liu, S.; Tang, H. Ultra-high specific strength Ti6Al4V alloy lattice material manufactured via selective laser melting. *Mater. Sci. Eng. A* **2022**, *840*, 142956. [CrossRef]
24. Tabie, V.M.; Li, C.; Saifu, W.; Li, J.; Xu, X. Mechanical properties of near alpha titanium alloys for high-temperature applications—A review. *Aircr. Eng. Aerosp. Technol.* **2020**, *92*, 521–540. [CrossRef]
25. Yang, J.; Song, Y.; Dong, K.; Han, E.-H. Research progress on the corrosion behavior of titanium alloys. *Corros. Rev.* **2023**, *41*, 5–20. [CrossRef]
26. Khorasani, A.M.; Goldberg, M.; Doeven, E.H.; Littlefair, G. Titanium in Biomedical Applications—Properties and Fabrication: A Review. *J. Biomater. Tissue Eng.* **2015**, *5*, 593–619. [CrossRef]
27. Dias Corpa Tardelli, J.; Bolfarini, C.; Cândido dos Reis, A. Comparative analysis of corrosion resistance between beta titanium and Ti-6Al-4V alloys: A systematic review. *J. Trace Elem. Med. Biol.* **2020**, *62*, 126618. [CrossRef]
28. Luo, X.; Yang, C.; Li, D.; Zhang, L.-C. Laser Powder Bed Fusion of Beta-Type Titanium Alloys for Biomedical Application: A Review. *Acta Metall. Sin. Engl. Lett.* **2024**, *37*, 17–28. [CrossRef]
29. Carrozza, A.; Aversa, A.; Fino, P.; Lombardi, M. A study on the microstructure and mechanical properties of the Ti-6Al-2Sn-4Zr-6Mo alloy produced via Laser Powder Bed Fusion. *J. Alloys Compd.* **2021**, *870*, 159329. [CrossRef]
30. Hassanin, H.; Zweiri, Y.; Finet, L.; Essa, K.; Qiu, C.; Attallah, M. Laser Powder Bed Fusion of Ti-6Al-2Sn-4Zr-6Mo Alloy and Properties Prediction Using Deep Learning Approaches. *Materials* **2021**, *14*, 2056. [CrossRef] [PubMed]
31. Peng, H.; Wu, S.; Kan, W.H.; Lim, S.C.V.; Zhu, Y.; Huang, A. Rapid hardening response of ultra-hard Ti-6Al-2Sn-4Zr-6Mo alloy produced by laser powder bed fusion. *Scr. Mater.* **2023**, *226*, 115209. [CrossRef]
32. Mouret, T.; Leclercq, A.; Brailovski, V. The LPBF printability and as-printed mechanical properties of a Ti6246 alloy as a function of printing parameters and microstructure. *Mater. Sci. Eng. A* **2025**, *946*, 149061. [CrossRef]
33. Carrozza, A.; Aversa, A.; Fino, P.; Lombardi, M. Towards customized heat treatments and mechanical properties in the LPBF-processed Ti-6Al-2Sn-4Zr-6Mo alloy. *Mater. Des.* **2022**, *215*, 110512. [CrossRef]
34. Carrozza, A.; Bircher, B.A.; Aversa, A.; Biamino, S. Investigating Complex Geometrical Features in LPBF-Produced Parts: A Material-Based Comparison Between Different Titanium Alloys. *Met. Mater. Int.* **2023**, *29*, 3697–3714. [CrossRef]
35. Aversa, A.; Carrozza, A.; Mercurio, V.; Calignano, F.; Sereda, O.; Pejchal, V.; Lombardi, M. A Comparison Between the Residual Stresses of Ti6Al4V and Ti-6Al-2Sn-4Zr-6Mo Processed by Laser Powder Bed Fusion. *Materials* **2025**, *18*, 689. [CrossRef]
36. Brika, S.E.; Letenneur, M.; Dion, C.A.; Brailovski, V. Influence of particle morphology and size distribution on the powder flowability and laser powder bed fusion manufacturability of Ti-6Al-4V alloy. *Addit. Manuf.* **2020**, *31*, 100929. [CrossRef]
37. *ASTM E9-09*; Test Methods of Compression Testing of Metallic Materials at Room Temperature. ASTM: West Conshohocken, PA, USA, 2010. [CrossRef]
38. *ISO 21920-2:2021*; Geometrical Product Specifications (GPS)—Surface Texture: Profile—Part 2: Terms, Definitions and Surface Texture Parameters. International Organization for Standardization: Geneva, Switzerland, 2021.
39. Pauzon, C.; Raza, A.; Hanif, I.; Dubiez-Le Goff, S.; Moverare, J.; Hryha, E. Effect of layer thickness on spatter properties during laser powder bed fusion of Ti–6Al–4V. *Powder Metall.* **2023**, *66*, 333–342. [CrossRef]
40. Zheng, H.; Li, H.; Lang, L.; Gong, S.; Ge, Y. Effects of scan speed on vapor plume behavior and spatter generation in laser powder bed fusion additive manufacturing. *J. Manuf. Process.* **2018**, *36*, 60–67. [CrossRef]
41. Tang, P.; Wang, S.; Duan, H.; Long, M.; Li, Y.; Fan, S.; Chen, D. The Formation of Humps and Ripples During Selective Laser Melting of 316l Stainless Steel. *JOM* **2020**, *72*, 1128–1137. [CrossRef]
42. Tang, C.; Le, K.Q.; Wong, C.H. Physics of humping formation in laser powder bed fusion. *Int. J. Heat Mass Transf.* **2020**, *149*, 119172. [CrossRef]
43. Masiagutova, E.; Cabanettes, F.; Sova, A.; Cici, M.; Bidron, G.; Bertrand, P. Side surface topography generation during laser powder bed fusion of AlSi10Mg. *Addit. Manuf.* **2021**, *47*, 102230. [CrossRef]

44. Hassanin, H.; El-Sayed, M.A.; Ahmadein, M.; Alsaleh, N.A.; Ataya, S.; Ahmed, M.M.Z.; Essa, K. Optimising Surface Roughness and Density in Titanium Fabrication via Laser Powder Bed Fusion. *Micromachines* **2023**, *14*, 1642. [CrossRef]
45. Wu, A.; Shi, Y.; Jing, Y.; Li, S.; Li, W.; Su, X. Effects of linear energy density on melt pool and microstructure of selective laser melted AlSi10Mg: An experimental and numerical study. *Mater. Today Commun.* **2025**, *43*, 111703. [CrossRef]
46. Lee, H.; Song, Y.; Yim, S.; Aoyagi, K.; Chiba, A.; Lee, B. Influence of linear energy on side surface roughness in powder bed fusion electron beam melting process: Coupled experimental and simulation study. *Powder Technol.* **2023**, *418*, 118292. [CrossRef]
47. Kasperovich, G.; Becker, R.; Artzt, K.; Barriobero-Vila, P.; Requena, G.; Haubrich, J. The effect of build direction and geometric optimization in laser powder bed fusion of Inconel 718 structures with internal channels. *Mater. Des.* **2021**, *207*, 109858. [CrossRef]
48. Solyaev, Y.; Rabinskiy, L.; Tokmakov, D. Overmelting and closing of thin horizontal channels in AlSi10Mg samples obtained by selective laser melting. *Addit. Manuf.* **2019**, *30*, 100847. [CrossRef]
49. Baier, M.; Sinico, M.; Witvrouw, A.; Dewulf, W.; Carmignato, S. Unravelling the dependency of dross formations in metal additively manufactured channels as a function of channel diameter and inclination angle. *CIRP J. Manuf. Sci. Technol.* **2023**, *45*, 69–81. [CrossRef]
50. Zhang, T.; Zhou, X.; Wang, D.; An, Z.; Ding, G.; Gao, H.; Bian, D. Mechanism of double exposure strategy for improving down-skin roughness and dimensional accuracy in support-free printing. *Mater. Des.* **2025**, *254*, 113990. [CrossRef]